
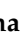


Article

Hydrogenation of Simulated Bio-Syngas in the Presence of GdBO₃ (B = Fe, Co, Mn) Perovskite-Type Oxides

Tatiana F. Sheshko ^{1,*} , Polina V. Akhmina ¹, Liliya G. Skvortsova ¹, Elizaveta M. Borodina ¹,
Tatiana A. Kryuchkova ¹, Irina A. Zvereva ²  and Alexander G. Cherednichenko ¹

¹ Department of Physical and Colloidal Chemistry, Faculty of Science, RUDN University, 6 Miklukho-Maklaya Street, 117198 Moscow, Russia; kryuchkova-ta@rudn.ru (T.A.K.)

² Department of Chemical Thermodynamics and Kinetics, Institute of Chemistry, Saint Petersburg State University, 7/9 Universitetskaya nab., 199034 Saint Petersburg, Russia

* Correspondence: sheshko-tf@rudn.ru

Abstract: Direct light olefin synthesis from bio-syngas hydrogenation is a promising pathway to decarbonize the chemical industry. The present study is devoted to the investigation of co-hydrogenation of carbon oxides in the presence of complex systems with the perovskite structure GdBO₃ (B = Fe, Mn, Co). The catalyst samples were synthesized by sol-gel technology and characterized by XRD, XPS, BET and TPR. It was found that the Fe/Mn-containing samples exhibited efficient catalysis of the hydrogenation of simulated bio-syngas to light hydrocarbons. The GdMnO₃ catalyst exhibits selectivity for C₂–C₃ light olefins of up to 37% among C₁+ hydrocarbons, with a maximum olefin/paraffin ratio. GdMnO₃ also exhibits high conversion of CO and CO₂, reaching up to 70–75% at 723 K. However, the GdFeO₃ catalyst shows a lower selectivity of (C₂–₃ = 22%, while it exhibits a higher conversion of CO₂, up to 95%, at the same temperature. Herein, we established a catalyst structure–performance relationship as a function of chemical composition. Oxygen mobilities and ratios of surface (O_s) to lattice (O_l) oxygen, forms of hydrogen adsorption, formation of -CH_x- radicals and their subsequent recombination to olefins are influenced by the nature of the element in the B position. This work provides valuable insights for the rational design of bimetallic catalysts for bio-syngas hydrogenation.

Keywords: hydrogenation; carbon oxides; perovskite catalysts; olefins; bio-syngas



Academic Editor: Pedro B. Tavares

Received: 6 December 2024

Revised: 7 January 2025

Accepted: 9 January 2025

Published: 13 January 2025

Citation: Sheshko, T.F.; Akhmina, P.V.; Skvortsova, L.G.; Borodina, E.M.; Kryuchkova, T.A.; Zvereva, I.A.; Cherednichenko, A.G. Hydrogenation of Simulated Bio-Syngas in the Presence of GdBO₃ (B = Fe, Co, Mn) Perovskite-Type Oxides. *Catalysts* **2025**, *15*, 67. <https://doi.org/10.3390/catal15010067>

Copyright: © 2025 by the authors. Licensee MDPI, Basel, Switzerland. This article is an open access article distributed under the terms and conditions of the Creative Commons Attribution (CC BY) license (<https://creativecommons.org/licenses/by/4.0/>).

1. Introduction

Over the past few centuries, the use of carbon-based fossil fuels—coal, oil and natural gas—has fueled a period of unparalleled human wealth and progress [1]. However, the concentration of carbon dioxide in the atmosphere is steadily increasing. The “greenhouse effect” is causing rising temperatures and contributing to global climate change. Countries are therefore forced to limit CO₂ emissions, and scientists are forced to develop efficient systems to capture and use CO₂ [2–4].

The conversion of biomass-derived syngas into chemicals and fuels using the Fischer-Tropsch (FTS) method is a promising way to create environmentally friendly and sustainable technologies for the production of fuels from renewable sources [5–8]. However, synthesis gas produced from biomass contains a significant amount of carbon dioxide (10–35% by volume), which is associated with the high oxygen content in the feedstock. This reduces the efficiency of the FTS process, which usually requires an optimal H₂/CO ≈ 2 ratio [9,10].

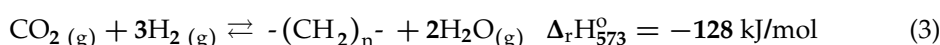
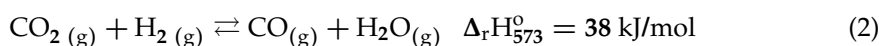
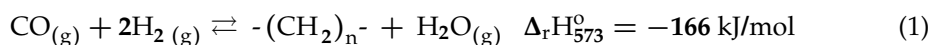
Therefore, methods for removing excess CO₂ from synthesis gas using additional devices have been developed [11,12]. Nevertheless, these actions raise the expenses for raw material processing, consequently increasing the price of the final product [13].

Bio-syngas is proving to be an attractive C₁ building block to produce high-value organic chemicals, as it is an economical, safe and renewable carbon source [5]. However, CO₂ is not commonly used as a carbon source in modern laboratory and industrial applications. In fact, only a few industrial processes—the synthesis of urea and its derivatives, salicylic acid and carbonates—use CO₂ as a chemical feedstock. This is mainly due to the thermodynamic stability of CO₂. The conversion of CO₂ into other chemicals usually requires high-energy substances or electro-reduction processes [14,15].

Much attention has been given by the scientific community to the direct hydrogenation of captured CO₂ and the production of value-added chemical products using carbon-free “green hydrogen” in the production process [16–21]. Catalysts for hydrogenating carbon oxides to methanol and olefins have been studied extensively. However, the direct hydrogenation of CO₂ to produce olefins is challenging due to the limitations of CO₂ inertness and the difficulty of chain growth [17,22,23].

Direct hydrogenation of CO₂ to -CH₂- is possible by dissociative adsorption followed by hydrogenation, but the extent of this process is unknown [24,25]. Another possible route is the direct Fischer–Tropsch synthesis of CO₂ and H₂ (CO₂-FT) by performing a reverse water–gas shift (RWGS) reaction followed by FT in the same reactor. This is thermodynamically simpler than RWGS, because the whole process is exothermic [26].

In general, three moles of H₂ are required to convert one mole of CO₂ to the hydrocarbon precursor -CH₂-, as shown in Equations (1)–(3) for the FTS and RWGS reactions, respectively. In particular, the RWGS reaction is a thermodynamically controlled reaction. Temperature and CO₂ concentration can shift the equilibrium forward or backward [24].



Thus, for the hydrogenation of CO₂ via FTS, it is desirable for the RWGS reaction to occur only after a certain concentration of CO₂.

The CO₂-FT process is very attractive as a route to producing alkanes and olefins straight from CO + CO₂ and H₂, but developing catalysts that are water-stable and highly selective for olefins is a daunting issue. A major problem limiting the selective conversion of CO₂ is the precise control of carbon chain growth to achieve high selectivity for hydrocarbons with the desired carbon series or bond structure (saturated, unsaturated, branched, etc.). As a thermodynamically stable molecule, CO₂ requires initial reduction to the intermediate CO and subsequent C–C coupling, in contrast to CO hydrogenation. This requires active sites corresponding to both RWGS and C–C coupling. As a result, these problems make the hydrogenation of CO₂ to olefins a more difficult process than FTS.

The most commonly used metals in a typical syngas (CO + H₂) FTS are Fe at high temperatures and Co at low temperatures. When comparing CO and CO₂ FTS, the conversion of CO is much higher than that of CO₂ [26]. In addition, high methane production and deviation from the Anderson–Schulz–Flory (ASF) distribution occur with Co-based catalysts in CO₂-FT [27]. New and improved catalysts for the synthesis of typical FT products using CO₂ as a carbon source therefore need to be investigated. Current research into CO₂-FT has focused mainly on Fe-based catalysts. These yield more olefins than Co-based catalysts. Olefin synthesis is also enhanced, and methane formation suppressed, by the addition of manganese (Mn) to an iron-based catalyst [28].

In recent times, perovskites have gained significant recognition as a viable substitute for a variety of catalytic systems. Their affordability, straightforward production process and the versatility of their structure through element substitution are key factors contributing to this [29]. The A-site metal in perovskites not only has a strong effect on the stability of the whole crystal configuration but also provides the possibility to improve catalyst performance by synergetic interactions with metals on the B-site [30,31]. For this reason, it is necessary to choose suitable metal ions on the A-site in this kind of structure.

In our previous work [32], the catalytic activity of complex oxides of the perovskite type $AFeO_3$ ($A = La, Nd, Gd, Ho, Yb, Lu$) in the dry reforming of methane was investigated. The results indicate the presence of a “gadolinium angle” in the values of product formation rate, which is associated with the peculiarities of electronic configuration change in the lanthanide series. Gadolinium inhibited the reduction of Fe^{3+} and Fe^{2+} in all types of catalysts, which then suppressed the formation of iron carbides during the reaction [31,32]. This increased the activity of the catalyst.

The present study investigates the effect of metal (Fe/Co/Mn) in the B-position of $GdBO_3$ perovskite catalysts for the conversion of CO_2 -rich syngas. Catalyst efficiency in terms of conversion and selectivity to different products was investigated at different CO_2 contents ($H_2/CO/CO_2$) in the feed. Since biomass-derived syngas is an H_2 -deficient feedstock for the FTS process, the experiments were performed under H_2 -deficient conditions [33]. The balanced H_2 content is defined as the molar ratio $H_2/(2CO + 3CO_2) = 1$ that is necessary for the production of one unit of the intermediate product $-(CH_2)-$. This ratio was obtained using Equations (1) and (3). In contrast, a raw material is called H_2 -deficient if the molar ratio of $H_2/(3CO_2 + 2CO)$ is 0.5 [34]. By varying the $CO_2/(CO_2 + CO)$ ratio from 0 to 1, experiments were carried out to investigate the effect of the presence of CO_2 in the feedstock under H_2 -deficient conditions. We have found that catalysts with a perovskite structure are promising for the FTS reaction in our previous studies [35–37]. It is therefore interesting to investigate the efficiency of $GdBO_3$ ($B = Fe, Co, Mn$) perovskite catalysts for converting CO_2 -rich syngas to light olefins. As a result, the optimum operating conditions for the conversion of CO_2 -rich syngas to obtain the maximum amount of light olefins were proposed.

2. Results

2.1. Characterization of the Catalysts

The XRD patterns of fresh and spent perovskites are shown in Figure 1. XRD analysis of the fresh catalysts (Figure 1) showed that the perovskites present in all catalysts consist mainly of $GdFeO_3$ (PDF-ICDD 01-072-9908), $GdCoO_3$ (PDF-ICDD 00-025-1057) and $GdMnO_3$ (01-070-9199). The diffraction peaks have a slight shift in the parameters towards large angles 2θ during the Fe–Mn–Co transition. This shift is associated with the difference in the radii of the B-ions and indicates the formation of structures with distorted crystal lattice parameters.

The investigation of the phase composition after the catalytic tests shows that during the catalytic transformations, the phase composition of $GdFeO_3$ remains unchanged, while the presence of C (PDF#00-041-1487) is observed in the $GdMnO_3$ diffractogram. Also observed in the samples studied is the presence of SiO_2 (PDF#01-077-1725), which was used to prevent sintering of the catalyst surface. The crystal lattice parameters and the results of elemental analysis of the synthesized perovskites, which are presented in Table 1, show a good correlation with the literature data [38,39] and the calculated values.

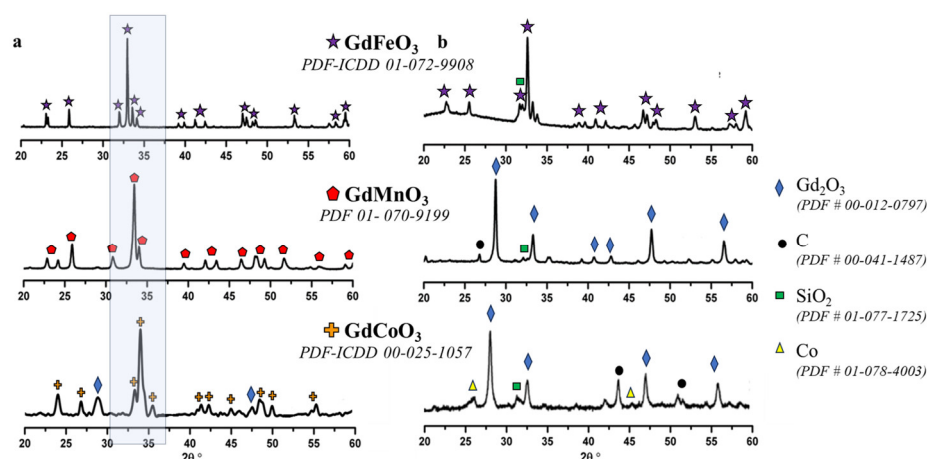


Figure 1. XRD patterns of the GdFeO₃, GdMnO₃ and GdCoO₃ oxides: (a) fresh; (b) spent.

Table 1. Structural parameters, surface composition by X-ray spectral microanalysis and specific surface area by BET of GdBO₃ compounds (B = Fe; Mn; Co).

Compound	Lattice Parameters (Å)	Crystallite Size (nm)	Space Group	Content (at%)			S _{BET} (m ² /g)
				Gd	B	O	
GdFeO ₃	a = 5.606 b = 7.671 c = 5.352	53.4	Pnma (62)	18.53	19.15	62.32	4.6
GdMnO ₃	a = 5.847 b = 7.435 c = 5.312	55.9	Pnma (62)	14.60	14.04	65.17	8.5

The specific BET surface areas of GdBO₃ are depicted in Table 1. The outcomes of the nitrogen adsorption–desorption technique are displayed in Figure S1. All the perovskite samples showcased the type IV isotherm based on IUPAC classification with an H1-type hysteresis loop. The IV isotherm characterizes parallel channels with cylindrical shapes in a mesoporous structure. Overall, two hysteresis loops can be identified in the isotherms. The first presented at an intermediate relative pressure (P/P_0) region, indicating a porous structure with uniform channels belonging to mesostructures. The second one at a relative pressure region of 0.8–1 implies textural mesoporous on GdBO₃.

The surface morphology of gadolinium ferrite, manganite and cobaltite was studied using scanning electron microscopy (Zeiss Merlin device, Oberkochen, Germany). The surface morphology of oxides with the composition GdBO₃ (B = Fe; Mn; Co) was studied using scanning electron microscopy. Micrographs of GdFeO₃ (a), GdMnO₃ (b) and GdCoO₃ (c) fresh and spent (d, f, e) catalysts are shown in Figure 2.

The metal substitution in the B-site of the perovskite structure slightly affected the morphology of the particles: for manganite and cobaltite, the particles turned out to be of “more regular” spherical shape with the crystallite size of 100–200 nm. However, their size was 55–60 nm according to XRD data, i.e., the particles obtained are polycrystalline formed by synthesis during calcination. As with ferrite, manganite and cobaltite had a porous structure, with larger particles having less marked porosity, consistent with the specific surface area (Table 1).

The investigation of surface morphology after catalytic tests showed that for all catalysts, a slight agglomeration of particles is observed, which is associated with some sintering of crystallites as a result of catalytic processes. Figure 2d–f shows that in addition to graphite, which is deposited directly on the catalyst surface according to the XRD and

TGA results, the formation of carbon with a “filamentary” structure similar to carbon nanotubes is observed.

Following the reaction, all the surface morphologies (Figure 2d–f) changed to reflect deformation and some aggregation of particles up to ~ 250 nm. The SEM micrographs of the used catalysts clearly showed that most of the surface was covered by deposited graphite and graphite clusters protruding on the surface, mixed with some fine filamentous carbon (Figure 2d–f). Graphite has been confirmed by TGA and XRD analyses. Particle growth did seem to occur on all three catalysts, but the carbon deposits are more severe for the GdCoO_3 catalysts (Figure 2e). For GdFeO_3 (Figure 2d) and GdCoO_3 (Figure 2e), in addition to graphite, the carbon structure also has a fibrous (filamentous) shape, similar to carbon nanotubes. This filamentous shape results from carbon diffusion through the crystal lattice of the catalytic system, and the formation and growth of filaments on the surface of the catalyst. This form does not cause deactivation of the catalysts and therefore does not affect their effectiveness. After reaction, no filamentous carbon was observed in all cases, since most of it would have been converted in situ to form a mixture of carbonates such as $\text{Gd}_2\text{O}_2\text{CO}_3$. XRD analysis showed the presence of $\text{Gd}_2\text{O}_2\text{CO}_3$ on the bulk of the GdCoO_3 surface.

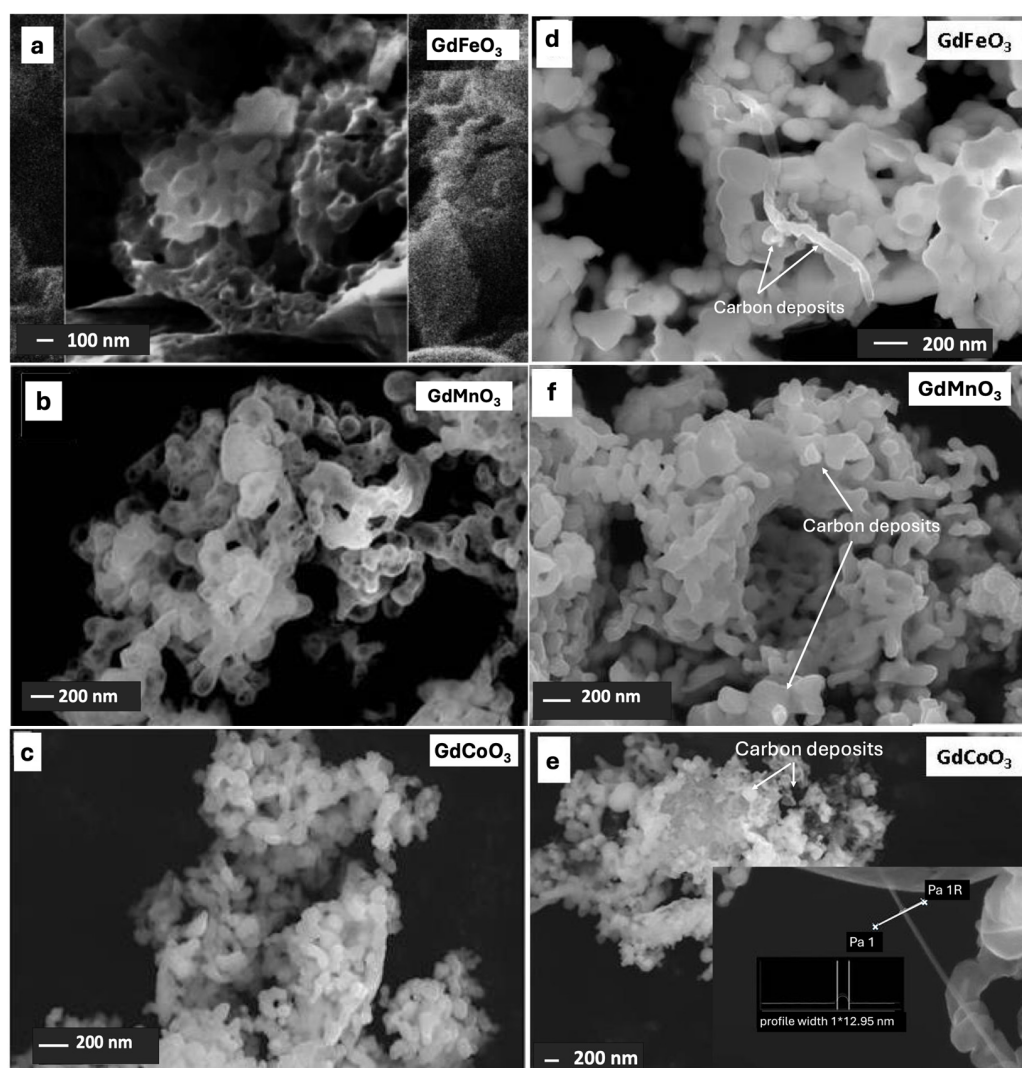


Figure 2. SEM images of the fresh (a–c) and spent (d–f) GdFeO_3 (a,d), GdMnO_3 (b,f) and GdCoO_3 (c,e) catalysts.

Overview XPS spectra (Figure 3) of GdFeO₃ (a), GdMnO₃ (b) and GdCoO₃ (c) demonstrate intense peaks of only Gd3d, Fe2p, Co2p, Mn2p, O1s and C1s in the binding energy range 0–1400 eV. The states of atoms were refined by decomposition of the spectra.

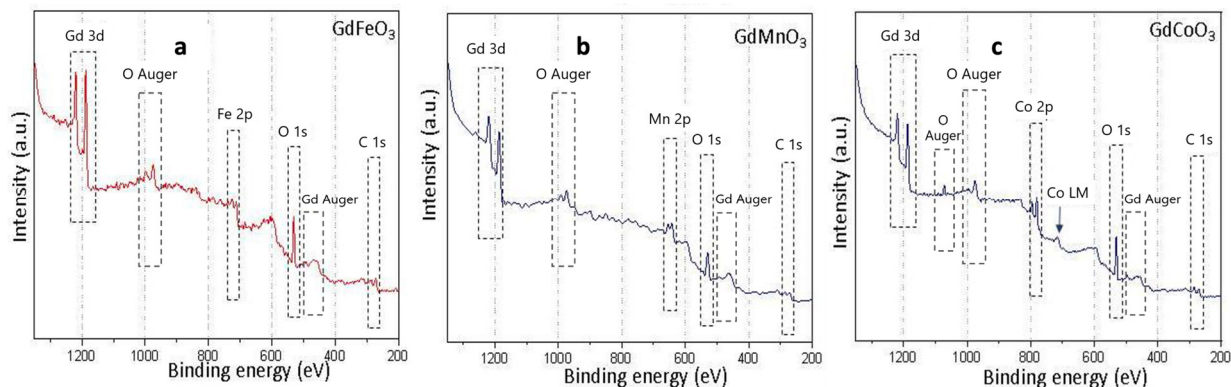


Figure 3. Survey XPS spectrum for compounds of the GdFeO₃ (a), GdMnO₃ (b) and GdCoO₃ (c), and identification of the main photoelectron lines.

The study of the XRS spectra of gadolinium for all oxides revealed the presence of peaks with binding energies at 141.6 and 1188.5 eV. These peaks are characteristic of Gd 4d_{5/2} and Gd 3d_{5/2}, corresponding to the Gd³⁺ state [40].

Analysis of the XPS spectrum of iron atoms showed that the curve represents a two-peak spectrum with low binding energy Fe2p_{3/2} and high binding energy Fe2p_{1/2} (Figure 4). The position of the Fe XPS peak depends on the chemical state and the environment of the atoms. The positions of Fe2p_{3/2} peaks for all studied oxides are in the range of 709.87 ~711.92 eV, and those of Fe2p_{1/2} peaks, 723.06~724.88 eV. The determined values of Fe2p_{3/2} and Fe2p_{1/2} peak positions correspond to the standard values for Fe²⁺ and Fe³⁺ states [41], and the presence of Fe in several states is also confirmed by the asymmetry of the Fe2p peaks [42].

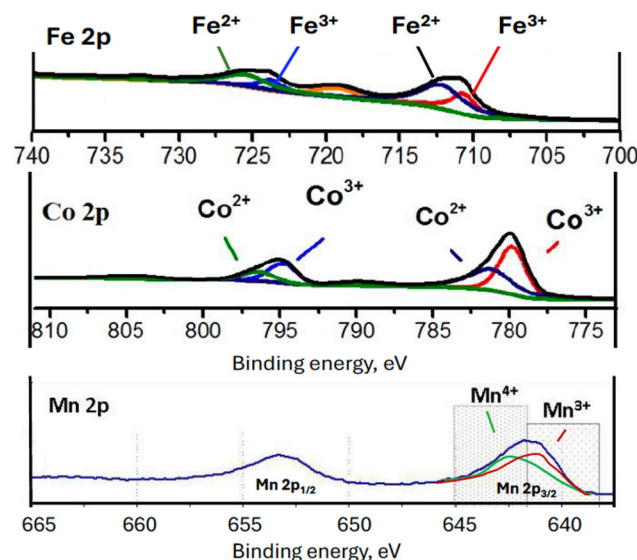


Figure 4. XPS spectra (Fe2p, Co2p and Mn2p region) of GdFeO₃, GdCoO₃ and GdMnO₃.

For GdCoO₃, the Co 2p spectra (Figure 4) are represented by two main and two “satellite” peaks, and the XPS spectra are broad, indicating the presence of atoms in several oxidation states. The main peaks, namely Co 2p_{3/2} and Co 2p_{1/2}, are located at binding energies of 779.80 eV and 795.1 eV, corresponding to Co²⁺ and Co³⁺ states, respectively [43]. The values of the spin–orbital splitting energies of Co 2p_{3/2} and Co 2p_{1/2} are ~15 eV.

Manganese, having six stable oxidation states (0, II, III, IV, VI and VIII), three oxidation states with significant multiplet splitting (II, III, IV), one oxidation state with less defined splitting or broadening (VI) and overlapping binding energy ranges for these multiplet splitting structures, presents a serious challenge for both qualitative and quantitative analysis [44]. The XPS spectra of Mn2p for GdMnO₃ (Figure 4) shows the presence of two peaks located at 641.8 eV (Mn 2p_{3/2} peak) and 653.4 eV (Mn 2p_{1/2} peak). The splitting between the Mn 2p_{3/2} and Mn 2p_{1/2} levels was 11.6 eV. The results (peak positions) are in good agreement with the literature data [44,45]. Based on the data for Mn 2p_{3/2}, the valence state of manganese in the compound is slightly higher than +3. Thus, the heterovalent state of manganese in the complex oxide GdMnO₃ is characterized by Mn³⁺ and Mn⁴⁺. This indicates that the manganite samples obtained have defects due to the lack of cations. Moreover, the Mn²⁺ state can also be present in complex oxides, but the task of determining the presence of this oxidation degree is complicated, because the XPS analysis binding energies of Mn 2p for the Mn²⁺, Mn³⁺ and Mn⁴⁺ states are quite close.

We note the presence of an O1s peak with a binding energy of around 528–532 eV in the XPS spectra (Figure 3). Figure 5 shows the O1s spectra for GdFeO₃, GdMnO₃ and GdCoO₃. The presence of two superimposed peaks for perovskite compounds has been reported [46,47]: the peak in the range of 528–530 eV corresponds to lattice oxygen (O_L), and the peak with binding energies of 530–532 eV corresponds to surface forms of oxygen (O_s): O²⁻, O₂²⁻ and O⁻. Each form can participate in the reaction and influence the catalytic properties [48]. The Table 2 summarizes the XPS data of the surface composition and atomic states of the studied perovskites.

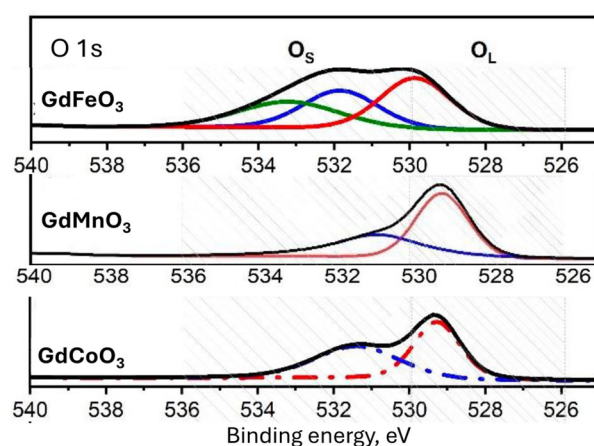


Figure 5. O1s spectra for GdFeO₃, GdMnO₃ and GdCoO₃.

Table 2. The XPS data of the surface composition and atomic states of the studied perovskites.

Compound	Content (at%)					
	Gd	B	B ²⁺ /(B ²⁺ +B ³⁺)	O _s	O _L	O _s /O _L
GdFeO ₃	23.60	16.32	0.64	36.27	23.80	1.52
GdMnO ₃	18.20	24.90	-	22.98	33.93	0.67
GdCoO ₃	18.19	21.99	0.47	26.61	32.21	0.83

2.2. Temperature-Programmed Reduction by Hydrogen

The reduction of perovskite-type oxides is thought to be stepwise and usually consists of two successive reduction stages: low temperature up to ~783 K and high temperature of 783–1273 K. According to the data described in [46], the low-temperature reduction region is associated with the Me³⁺ → Me²⁺ transition, while the broad reduction peaks in the high-temperature region are associated with the Me²⁺ → Me⁰ transition.

Figure 6 shows the H₂-TPR spectra of complex and simple Fe/Mn/Co oxides. The reduction of the B-element in perovskites occurs in two stages. The temperature ranges of these stages are shown in Table 3. The presence of the reduction peak in the first temperature range describes the partial reduction of Fe³⁺ → Fe²⁺, Mn⁴⁺ → Mn³⁺, Co³⁺ → Co²⁺ and the formation of an oxygen-deficient compound of the GdBO_{3-δ} type. The main peak of reduction to the metallic state for GdFeO₃ and GdCoO₃ falls in the high temperature range. This is due to the high stability of these compounds in a hydrogen atmosphere.

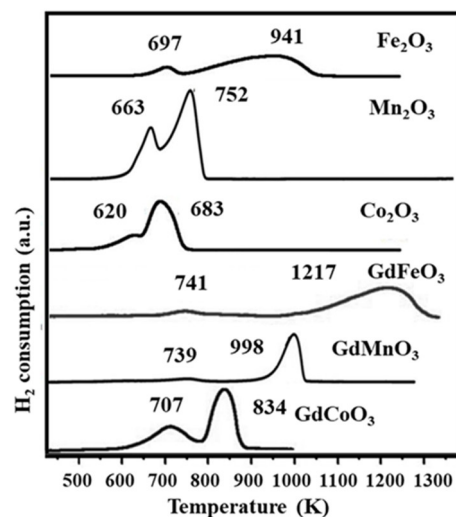


Figure 6. H₂-TPR curves of GdBO₃ (B = Fe, Mn, Co) and cobalt, manganese and iron oxides.

Table 3. Temperature reduction and quantitative analysis curves of temperature-programmed reduction of GdBO₃ (B = Fe, Mn, Co).

Oxides	Temperature (K)		H ₂ Consumption, mmol/g		
	Peak 1	Peak 1	Peak 1	Peak 1	Total
GdFeO ₃	741 K (Fe ³⁺ → Fe ²⁺)	1217 K (Fe ²⁺ → Fe ⁰)	141	752	893
GdMnO ₃	739 K (Mn ⁴⁺ → Mn ³⁺)	998 K (Mn ³⁺ → Mn ²⁺)	286	528	814
GdCoO ₃	707 K (Co ³⁺ → Co ²⁺)	834 K (Co ²⁺ → Co ⁰)	381	592	973

Two reduction ranges are also observed, but at lower temperatures, for the simple oxides Fe₂O₃, Mn₂O₃ and Co₂O₃. This means that the reduction of the B-element in the perovskite structure is more complicated than in simple oxides, which may be due to the mutual influence of Gd–O–B and the different oxygen environment of the B-atom.

The XRD data of the spent GdCoO₃ show its reduction to Gd₂Co₂O₅, and that the valence states of cobalt change from Co³⁺ to Co²⁺. These data are in good agreement with the results described in the literature [49]. Analysis of the phase composition of GdCoO₃ after the second reduction peak (~1173 K) shows the presence of Gd₂O₃ and Co phases, confirming the reduction of Co²⁺ to Co⁰.

The phase analysis study shows that GdCoO₃ after reduction exhibits the absence of diffraction peaks characteristic of perovskites, indicating the destruction of the perovskite structure and its transformation into Gd₂O₃ (PDF-ICDD 00-012-0797) and Co (PDF-ICDD 01-078-4003). As for GdFeO₃, the phase composition study shows the presence of GdFeO₃ perovskite phase reflections (PDF-ICDD 01-072-9908) and a small peak of Gd₂O₃ (PDF-ICDD 00-012-0797), which is related to the high recovery temperature of

this compound (peak at 1217 K, Figure 6). The first peak at ~ 739 K is associated with the reduction of Mn^{4+} to Mn^{3+} in GdMnO_3 , and those at temperatures above 973 K with the reduction of Mn^{3+} to Mn^{2+} [50]. In comparison with GdCoO_3 and GdFeO_3 , the process is accompanied by a lower level of hydrogen absorption.

For the Gd–Co–Mn–Fe–O series, the T_{max} of the reduction peaks is shifted to a higher-temperature region, which indicates a high thermal stability, possibly arising due to the influence of the mutual strengthening of the M–O bond ($M = \text{Co}, \text{Mn}, \text{Fe}$), which leads to a limitation of the mobility of oxygen ions.

2.3. Catalytic Activity

Figure 7 shows feedstock conversions at different values of $R = \text{CO}_2 / (\text{CO}_2 + \text{CO})$ for H_2 -deficient feedstock compositions.

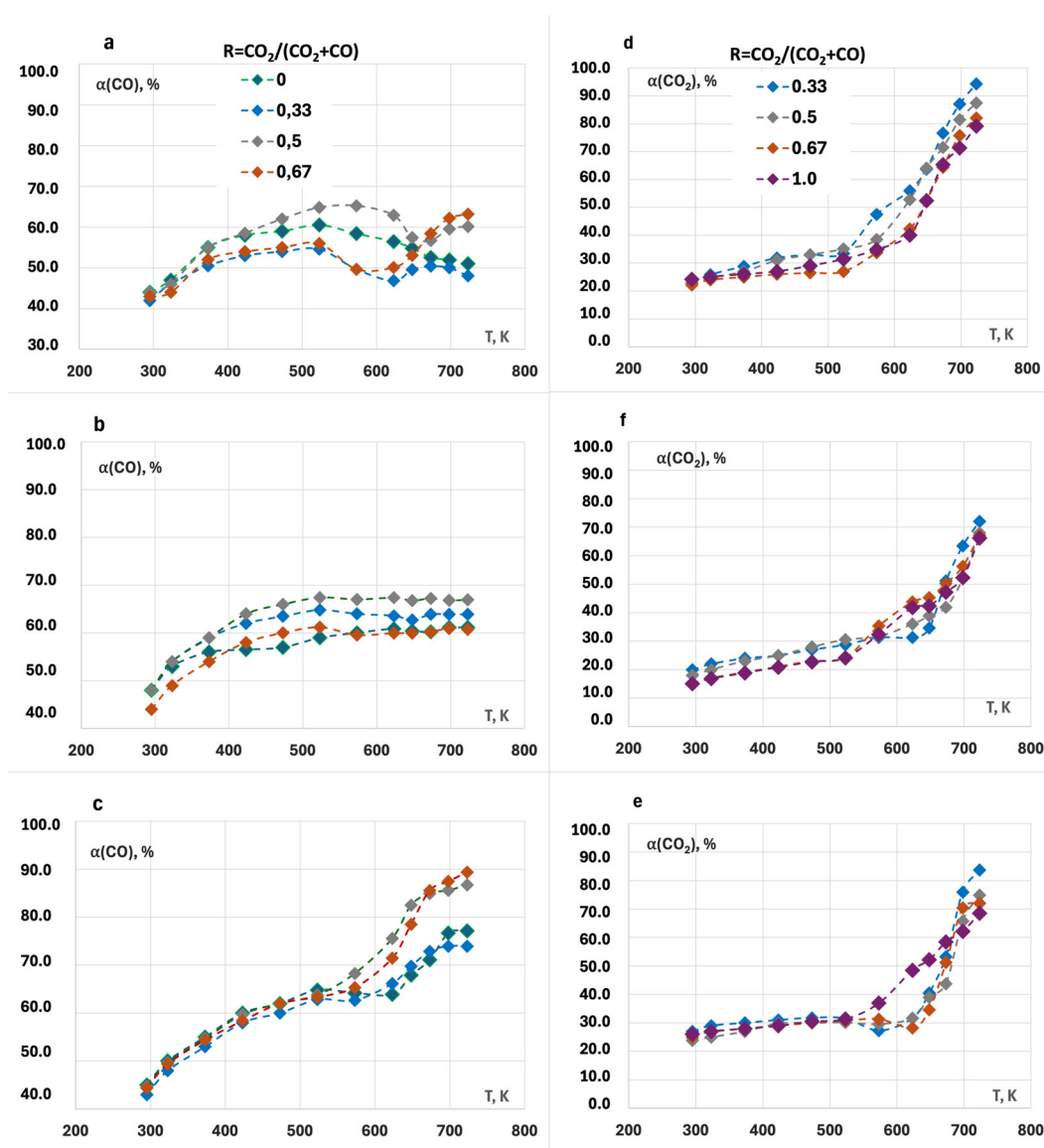


Figure 7. Temperature dependencies of CO (a–c) and CO_2 (d–f) conversion on GdFeO_3 (a,d), GdMnO_3 (b,f) and GdCoO_3 (c,e).

Under all conditions and on all catalysts investigated, the CO conversion was already above 40% at 293 K (Figure 7a–c) and increased with increasing temperature. However, on GdFeO_3 in the temperature range 573–673 K, a decrease in CO conversion was observed at all compositions of the reaction mixture. This can be explained by the formation of

CO because of the RWGS reaction, which is most intense on iron-containing catalysts and increases with increasing CO₂ concentration in the feed [51]. Under H₂-deficient conditions, the % CO conversion was maximal at CO₂/(CO + CO₂) = 0.5 for all complex oxides. It is noteworthy that the CO₂ conversion was not negative for all samples and increased from 10–15% at 293 K to 80–90% at 723 K (Figure 7d–f). CO₂ conversion occurs in two steps, where in the first step CO₂ is converted to CO via the RWGS reaction. As a result, the CO conversion either decreases or does not change (Figure 7). In a second step, the CO formed is converted into hydrocarbons by the FTS reaction. There is a value of critical ratio $RC = CO_2/(CO_2 + CO)$ [52], at which CO₂ conversion becomes equal to zero or even negative, which is associated with WGS. $RC = CO_2/(CO_2 + CO)$ varies between 0.35 and 0.75 on iron-containing catalysts, as shown in [34,53,54]. Syngas produced from biomass contains higher than critical amounts of CO₂. The hydrogenation of such bio-syngas does not require removal of CO₂ from the feedstock. This increases the carbon efficiency of the process. The positive CO conversion values at all CO₂/(CO₂ + CO) ratios indicate that our perovskite catalysts are highly active towards RWGS and show significant FTS reaction activity under these conditions.

The RWGS is an endothermic reaction, so it is favored at higher temperatures, whereas FTO is an exothermic process [55,56]. Therefore, thermodynamic data indicate that low temperature favors the FTO reaction, while a high temperature is necessary to activate CO₂ for the RWGS reaction [57,58]. Therefore, the reaction conditions greatly influence the CO₂ conversion and product distribution.

Figure 8 shows the distribution of hydrogenation products at 723 K as a function of $R = CO_2/(CO_2 + CO)$ of perovskites with different elements in the B-position. The product yield depends on the ratio of CO to CO₂. Indeed, the result showed a strong product dependency on the CO₂/(CO₂ + CO) ratio in the feed gas. In particular, the CO₂-rich feedstock favors the formation of linear-chain hydrocarbons, especially for GdCoO₃. These results agree with literature data using cobalt-based catalysts [54,59]. The low CO₂ concentration (less than 50%) acts as a diluting agent in the feed gas on cobalt catalysts. For GdFeO₃, increasing the CO₂ content in the feed gas suppressed the methane formation while decreasing the CO₂ conversion. High CO₂ concentration favors the RWGS reaction, and the main products were obtained by CO hydrogenation. However, CO₂ was converted to hydrocarbons at higher CO₂ concentration (more than 50%) and affected the overall distribution of FTS products. This can be explained by the change in the mean partial pressure of CO and H₂. The partial pressure of hydrogen (H₂) remains relatively constant, while a decrease in the partial pressure of carbon monoxide (CO) leads to an increase in the ratio of H₂ to CO at the surface. This, in turn, enhances the yield of C₂ and higher hydrocarbons. These findings are consistent with the trend observed in the iron (Fe/Cu/K/Si/Al) catalysts, where selectivity for longer-chain hydrocarbons increases as the CO₂ content of the feed gas increases [34,52].

Increasing the CO₂ content of the feed resulted in an increase in the propylene fraction when hydrogenation was carried out in the presence of GdMnO₃. Mn is a well-studied promoter in CO₂ hydrogenation via CO₂-FTS and is considered an effective option for altering the product [52,60,61]. Al-Dossari et al. [62] observed that the Mn promoter inhibits H₂ adsorption and increases the affinity for CO₂ due to its basicity, thereby reducing methane formation and increasing the O/p value and selectivity towards C₂₊ hydrocarbons.

Calculation of total selectivity for ethylene and propylene at different $R = CO_2/(CO_2 + CO)$ showed an increase with increasing temperature for all studied catalysts (Figure 9). The highest C_{2–3} values are achieved on GdMnO₃ (up to 35%) at T = 723 K and at R = 0.5. GdFeO₃ catalyst also shows high C_{2–3} selectivity, reaching 22% at 723 K, while the lowest selectivity for light olefins belongs to GdCoO₃ (4%).

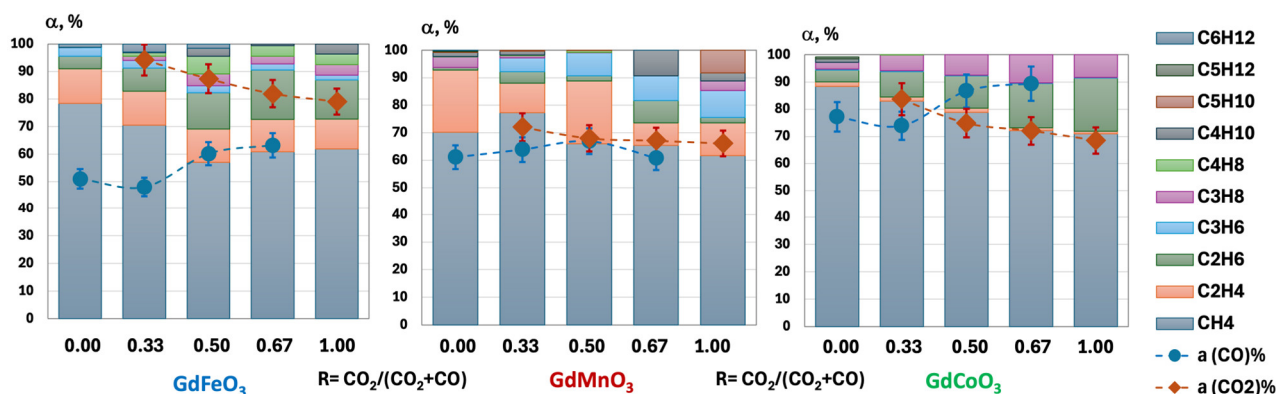


Figure 8. Distribution of hydrogenation products at 723 K from $R = \text{CO}_2/(\text{CO}_2 + \text{CO})$ for GdFeO_3 , GdMnO_3 and GdCoO_3 .

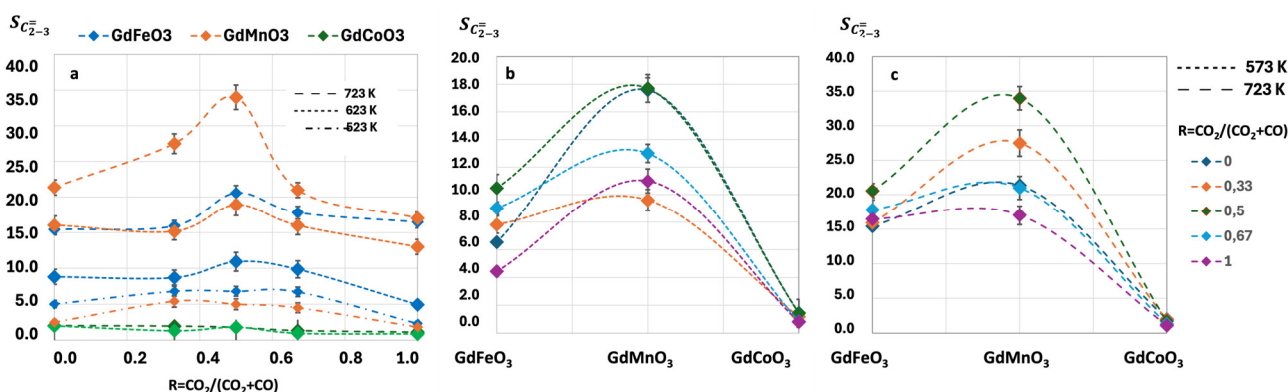


Figure 9. Selectivity for C_{2-3} olefins as a function of CO_2 content in the reaction mixture (a) on GdFeO_3 , GdMnO_3 and GdCoO_3 at 573 (b) and 723 K (c).

Figure 9 also shows that the C_{2-3} selectivity depends on the CO/CO_2 ratio. For GdFeO_3 and GdMnO_3 , increasing the ratio $R = \text{CO}_2/(\text{CO}_2 + \text{CO})$ up to 0.5 led to an increase in selectivity. At $R > 0.5$, the selectivity decreased and was comparable to the corresponding values for hydrogenation of carbon monoxide ($R = 0$) only. In the presence of GdCoO_3 , the increase of CO_2 content in the feed reduced the already low yield of olefins.

Kinetic parameters were determined from Arrhenius plots, charting effective activation energies of product formation and logarithms of the pre-exponent, characteristic of the number of active centers of the catalyst. The calculated corresponding values for all samples are presented in Table 4.

For the hydrogenation of carbon monoxide, the nature of the element in the B-position of the complex oxide structure does not significantly change the apparent activation energies of the hydrogenation product formation. The activation energies of methane, ethylene and propylene formation were comparable for GdFeO_3 and GdCoO_3 and were larger for GdMnO_3 . The apparent activation barrier was at a similarly low value of 30 ± 10 kJ/mol for CH_4 , C_2H_4 and C_3H_6 formation.

When the reaction was carried out in the presence of CO_2 , an increase in the CO_2 content led to a decrease in the E_a^* of methane, ethylene and propylene formation for the iron catalyst. Conversely, for cobaltite and manganite, an increase in $R = \text{CO}_2/(\text{CO}_2 + \text{CO})$ up to 1 led to an increase in the effective activation energies of product formation.

For all catalysts, the logarithm of the equilibrium constant for the reaction in the presence of carbon dioxide is greater than for the reaction with carbon monoxide alone. The CO_2 effect was most significant for GdMnO_3 . The increase in the logarithms of the pre-factor suggests the presence of some compensation effect (Meyer-Neidel rule [63]), which

manifests itself in heterogeneous catalytic reactions. Usually, this effect indicates that the process being studied is a multi-step process, and that the establishment of equilibrium is preceded by a so-called “pre-equilibrium” stage, e.g., adsorption equilibrium (dissociative adsorption of CO₂, CO and H₂; formation of surface carbonate complexes and CH particles) [37]. In the case of complex oxides GdBO₃, adsorption of CO and CO₂ predominantly occurs on the A-centers of perovskite [64,65] with the formation of carbonate complexes Gd₂O₂CO₃. The dissociative adsorption of both CO and CO₂ easily occurs in the case of co-hydrogenation of carbon oxides, leading to an increased concentration of CH_x particles and the interaction between them to produce ethylene and propylene.

Table 4. Values of activation energies and pre-exponential multipliers of the investigated catalysts for methane, ethylene and propylene.

R = CO ₂ /(CO ₂ + CO)	CH ₄		C ₂ H ₄		C ₃ H ₆	
	E _a , kJ/mol	lnK ₀	E _a , kJ/mol	lnK ₀	E _a , kJ/mol	lnK ₀
	GdFeO ₃					
0	30	4.74	34	6.37	44	5.94
0.33	22	6.28	29	7.07	39	6.70
0.50	22	6.45	30	7.01	38	7.20
0.67	21	6.57	28	7.32	38	7.26
1.00	20	6.52	28	7.60	42	6.79
	GdMnO ₃					
0	67	1.57	89	3.47	87	11.7
0.33	74	6.47	93	15.01	74	15.9
0.50	73	10.7	73	9.60	74	9.1
0.67	73	16.6	81	18.90	91	12.5
1.00	54	6.51	77	15.17	73	12.9
	GdCoO ₃					
0	33	2.15	36	5.74	35	7.13
0.33	38	1.48	46	4.19	43	6.27
0.50	39	1.08	46	3.80	45	5.43
0.67	38	1.79	43	5.23	41	6.98
1.00	31	2.94	35	6.89	40	7.35

The CO₂ pressure did not affect the kinetic characteristics of C₂–C₃₊ olefin formation on all these catalysts. The specific rate dependencies of CO₂ conversion and formation of carbon-containing products with respect to reactants are different for CO₂ hydrogenation on different catalysts, because the substitution of a metal atom in the B-position changes the reducibility of these catalysts and/or the identity of carbon species on the catalyst surface [66]. The reducibility of catalysts and/or the identity of the surface carbon species can affect the kinetically relevant steps, active site structures, the number of unoccupied Me atoms and hence the rate dependencies. It was reported in [67] that the oxophilicity of the catalyst surface can determine the degree of surface oxygen content and its involvement in kinetically significant stages of C–H activation. Modification of the oxophilicity of catalysts by substitution of the element in the B-position led to a change in their properties [67].

As discussed above, adsorption of both CO and CO₂ primarily occurs on the A-sites of perovskite, leading to the formation of carbonate complexes Gd₂O₂CO₃ [65]. In the studied perovskites, the lattice parameters of the crystal lattice are changed, and therefore the binding energy between oxygen and metal in Gd–O–Me is also changed, which in turn affects the gadolinium–oxygen bond and is reflected in the conversions of both CO and CO₂ and consequently in the product selectivity (Figure 10).

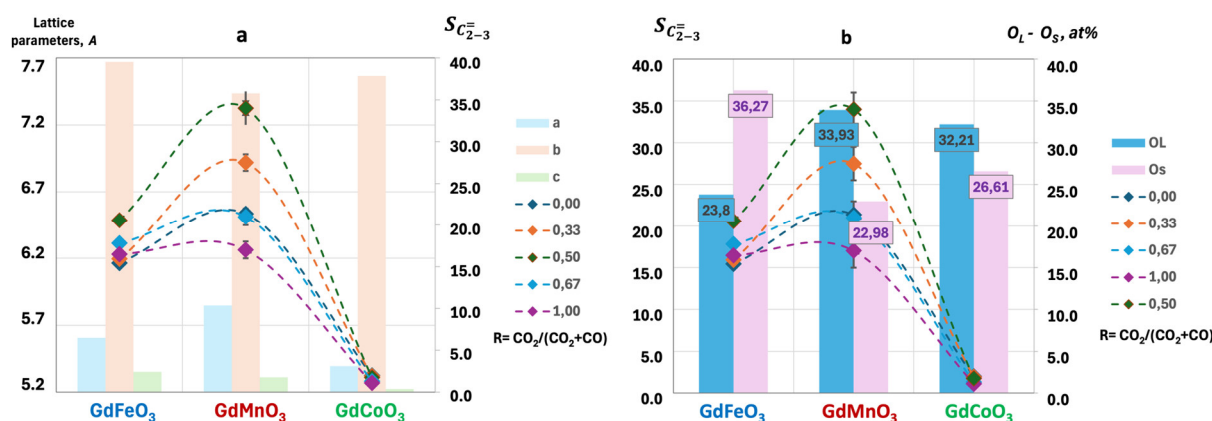


Figure 10. Selectivity for C₂–C₃ olefins and crystal lattice parameters (a); the proportion of surface oxygen (O_s) and lattice oxygen (O_l) (b).

As shown in [68], the type of element in the B-position affects the mobility of oxygen and redox properties, and also changes the ratio of surface to lattice oxygen in the structure of complex oxides. Thus, the substitution of iron for cobalt or manganese leads to a decrease in the fraction of surface oxygen O_s and an increase in the fraction of lattice O_l. Experimental results indicate that with increasing temperature, not only surface but also lattice oxygen starts to participate in the reaction, the amount of which depends on the oxide composition, i.e., the oxidizing capacity of the samples increases in the series GdFeO₃ < GdCoO₃ < GdMnO₃ (Figure 10).

The RWGS reaction proceeds mainly via surface carbonate intermediates, including reaction between the surface carbonates and oxygen vacancies or the diffusion of the vacancies [69]. Theoretical studies using model systems of the RWGS reaction mechanism predicted that C–O bond breaking in CO₂ occurred prior to the dissociation of H₂ [70]. The H₂ moiety could promote the charge transfer in the Me insertion process and facilitate the dissociation of coordinated CO₂ molecules by reducing the energy barrier. The rate-determining step for the reaction is the migration of the hydrogen atom from the Me center to the oxygen atom. As the metal radius increases, the overlap of filled orbitals decreases, and the binding energy of the atoms increases in the Mn–Fe–Co series. Therefore, it is expected that dissociation will be easier with decreasing d-orbital filling and decreasing atomic radius. It can be assumed that exactly Co³⁺, Mn³⁺ and Fe³⁺ in the Gd–O–Me bond are active centers for hydrogen adsorption. Hydrogen is known to be preferentially adsorbed and dissociative in atomic form on the surface of manganese and iron, and on cobalt in both molecular and dissociative forms [71]. The ratio between saturated and unsaturated hydrocarbons in hydrogenation products is also determined by the amount of atomic hydrogen able to migrate from some active surface sites to others and by the structure of these sites [36]. This is in good agreement with the experimental data obtained: comparable selectivity for olefins on GdFeO₃ and GdMnO₃ and low selectivity on GdCoO₃.

When examining the specifics of the process of producing light olefins, it becomes evident that maintaining the correct balance between active H and C is crucial [72]. The large amount of *H on the surface (* denotes the adsorption state) will result in excessive hydrogenation, which can lead to methanation. Conversely, if there is not enough H on the surface, the catalyst will not be able to hydrogenate effectively, reducing its ability to convert CO₂.

CO₂ is first adsorbed and activated on the active Gd–O centers of perovskite to form carbonate complexes Gd₂O₂CO₃. Hydrogen is adsorbed dissociatively/molecularly on the B–O–B centers. Then, *CO₂ can be hydrogenated by adsorbed *H to form an intermediate compound *HOCO. The intermediate compound then dissociates into *OH and *CO. The

*CO is then either desorbed as CO or undergoes further reactions through successive FTS. To form hydrocarbons, *CO can dissociate into *C and *O [72,73]. The *C can then be hydrogenated to *CH_x at the surface. The *CH_x species are precursors to the formation of olefins. The most likely pathways are the accession of *C + *CH_x and *CH_x + *CH_x [72]. Alternative partial hydrogenation of CO to HCO seems unlikely, as oxygenates were not present in the reaction products. In short, the main stages in the conversion of CO₂ into light olefins involve the breaking of C–O bonds and the formation of C–C bonds. A unique aspect of this proposed process is that there is no stage for carbide formation. X-ray analysis of the spent catalysts did not detect their presence. The structure of the catalyst framework and the presence of gadolinium prevent the formation of iron carbides, thus increasing the activity of the catalyst [31].

3. Materials and Methods

3.1. Materials

Iron, cobalt and gadolinium nitrates (Fe(NO₃)₃·9H₂O, 98.5% AR; Co(NO₃)₃·9H₂O, 98.5% AR; Gd(NO₃)₃·6H₂O, 99.9% AR) were supplied from Vekton, St. Petersburg, Russia. Manganese nitrate (Mn(NO₃)₂·6H₂O, 98% AR) was purchased from Lenreactiv, St. Petersburg, Russia. Citric acid was purchased from ALDOSA, Moscow, Russia, and was of analytical grade (AR, 99.3%). All chemicals were used as received without further purification.

3.2. Catalyst Preparation

The citrate–nitrate sol-gel method [74,75] was used for the synthesis of complex oxides. A twofold excess of citric acid was added to solutions containing stoichiometric amounts of nitrates under constant stirring. The synthesis was carried out at pH = 6. The resulting sol was heated to 393 K and kept at this temperature until a dark porous dry gel was formed. The gel was then calcined at a gradual increase in temperature to 723 K for 2 h. Gadolinium cobaltite required additional calcination at 1073 K for one hour.

3.3. Characterization

X-ray diffraction (XRD) analysis was carried out using the Rigaku MiniFlex II diffractometer (Tokyo, Japan). The operating voltage and current were 30 kV and 15 mA, respectively, and the scanning range was $2\theta = 10\text{--}60^\circ$. The Cu-K α radiation source was used, and the spectra were recorded at a scan rate of $5^\circ/\text{min}$. The ICDD-PDF2 database was used to analyze the phase composition of the studied samples.

X-ray photoelectron spectra (XPS) were recorded by Thermo Fisher Scientific (Waltham, MA, USA) Escalab 250Xi spectrometer (AlK α = 1486.6 eV, spectral resolution 0.5 eV). The C1s peak of 284.6 eV was used as the calibration peak to correct the charge effect of the sample.

Temperature-programmed reduction (TPR) was conducted using a Micromeritics AutoChem II 2920 analyzer (Micromeritics Instrument Corporation, Norcross, GA, USA). In each H₂-TPR test, 50 mg of catalyst was used. The materials were loaded into a U-shaped continuous-flow quartz reactor and heated up to 1273 K at a 10 K/min rate in 10% H₂/Ar gas mixture passed at a flow rate of 50 mL/min. Water vapors were captured using a trap placed in a Dewar with ethyl alcohol (T = 134 K). Hydrogen consumption was measured by TCD (thermal conductivity detector).

Thermogravimetric analysis (TGA) was performed by NETZSCH (Exton, PA, USA) STA 449 F5 in the temperature range of 303 to 1173 K (heating rate of 10 K/min) in a stream of air (rate = 50 mL·min^{−1}).

Scanning electron microscopy (SEM) and energy-dispersive X-ray (EDS) analyses were conducted via a Zeiss Merlin system (Oberkochen, Germany).

N₂ adsorption–desorption measurement was conducted using Quadrasorb SI device (Boynton Beach, FL, USA) at the liquid nitrogen temperature of 77 K. The specific surface area was calculated using the Brunner–Emmett–Teller (BET) method.

3.4. Catalytic Activity Tests

Catalytic tests were carried out in a flow reactor at atmospheric pressure, in the temperature range of 523–708 K and a feed volume rate of 1.5 L/hour (GHSV = 8700 h^{−1}) with component ratio [(CO + CO₂):H₂] = 1:2, [CO₂/(CO + CO₂)] = 0 ÷ 1.

Powdered catalysts (0.1 g) were mixed with fine-grained quartz (d_{mid} = 1–10 μm) in a ratio of 1:5 to avoid sintering and placed in a quartz reactor (d_{reactor} = 1 cm) with a quartz filter to avoid particulate entrainment.

The reactants were analyzed by a Chromatec Crystal 5000 gas chromatograph (Yoshkar-Ola, Russia) equipped with a column of stainless steel filled with Porapak Q and TCD and FID detectors (with argon as a carrier gas). The rate of product formation R_i (mol/hour·g) was measured after reaching a steady state.

The catalytic characteristics were calculated using the following equations:

$$\alpha_i, \% = \frac{n_{\text{int}} - n_{\text{out}}}{n_{\text{int}}} \times 100 \quad (4)$$

$$S_i, \% = \frac{R_i}{\sum R_i} \times 100 \quad (5)$$

$$R_i = \frac{n_{i\text{out}}\omega}{V_m} \quad (6)$$

where n_{in} and n_{out} are the component molar content in the input and output of the reactor, respectively; ω is the feed rate (L/h); V is the chromatograph loop volume (0.153×10^{-3} L); and m is the catalyst mass (g).

4. Conclusions

To summarize, we synthesized a series of GdBO₃ (B = Fe, Mn, Co) perovskite-type catalysts and found that Fe/Mn-containing samples efficiently catalyzed the hydrogenation of simulated bio-syngas to light hydrocarbons. Increasing the carbon dioxide content of the reaction mixture to CO₂/[CO + CO₂] = 0.5 suppressed the formation of methane and favored the formation of light olefins. The hydrogenation of CO₂ occurred by combining the primary reverse water–gas shift reaction to form CO and the subsequent hydrogenation of CO to produce olefins and paraffins. The GdMnO₃ catalyst exhibits selectivity for C_{2–3} of up to 37% among C₁₊ hydrocarbons, with a maximum olefin/paraffin ratio. GdMnO₃ also exhibits high conversion of CO and CO₂, reaching up to 70–75% at 723 K. However, the GdFeO₃ catalyst shows a lower selectivity of C_{2–3} = 22%, while it exhibits a higher conversion of CO₂ up to 95% at the same temperature. Herein, we established a catalyst structure–performance relationship as a function of chemical composition. Substitution of an element in the B-position leads to a change in oxygen mobility and the ratio of surface oxygen (O_s) to lattice oxygen (O_l). This is reflected in the conversion of carbon oxides as they are adsorbed on A-centers via surface oxygen. The nativity of the element in the B-position also influences the forms of hydrogen adsorption, the formation of -CH_x- radicals and their subsequent recombination into olefins. The process of converting bio-syngas into light olefins involves breaking C–O bonds and forming C–C bonds. The uniqueness of the proposed technique lies in the fact that it does not lead to the formation of carbides. The analysis of spent catalysts did not reveal their presence. The framework structure and the

presence of gadolinium prevent the formation of iron carbides, which, in turn, increases the activity of the catalysts.

The findings presented here provide a strategy to tune bio-syngas hydrogenation product distributions toward specific target products by varying the catalyst composition. Further detailed studies are needed to identify the active sites/phase and elucidate the underlying mechanisms, given the complexity of perovskite catalytic systems.

Supplementary Materials: The following supporting information can be downloaded at: <https://www.mdpi.com/article/10.3390/catal15010067/s1>, Figure S1: N₂ adsorption/desorption isotherms of GdFeO₃(a), GdMnO₃(b) and GdCoO₃(c).

Author Contributions: Conceptualization and methodology, I.A.Z. and T.F.S.; investigation, P.V.A., L.G.S., T.A.K. and E.M.B.; data curation, T.A.K.; writing—original draft, E.M.B., P.V.A., L.G.S. and T.A.K.; writing—review and editing, T.A.K., T.F.S. and I.A.Z.; supervision, A.G.C.; project administration, A.G.C.; funding acquisition, T.F.S. All authors have read and agreed to the published version of the manuscript.

Funding: This work was funded by the Russian Science Foundation, grant no. 24-29-00341, <https://rscf.ru/project/24-29-00341> (accessed on 1 January 2024).

Data Availability Statement: Original data are available from authors E.M.B., T.A.K. and T.F.S.

Acknowledgments: The authors are grateful to Saint Petersburg State University Research Park. The XRD study was carried out at the Research Center for X-ray Diffraction Studies, and the XPS study was performed at the Resource Center for Studies in Surface Science. TG analysis was carried out at the Center of Thermal Analysis and Calorimetry.

Conflicts of Interest: The authors declare no conflicts of interest. The funders had no role in the design of the study; in the collection, analyses or interpretation of data; in the writing of the manuscript; or in the decision to publish the results.

References

1. Olah, G.A.; Goepfert, A.; Prakash, G.K.S. Chemical Recycling of Carbon Dioxide to Methanol and Dimethyl Ether: From Greenhouse Gas to Renewable, Environmentally Carbon Neutral Fuels and Synthetic Hydrocarbons. *J. Org. Chem.* **2008**, *74*, 487–498. [[CrossRef](#)] [[PubMed](#)]
2. Riduan, S.N.; Zhang, Y. Recent Developments in Carbon Dioxide Utilization under Mild Conditions. *Dalton Trans.* **2010**, *39*, 3347. [[CrossRef](#)] [[PubMed](#)]
3. Nomoto, K.; Okazaki, T.; Beppu, K.; Shishido, T.; Amano, F. Highly Selective Formate Formation *via* Bicarbonate Conversions. *EES. Catal.* **2024**, *2*, 1277–1284. [[CrossRef](#)]
4. Hirunsit, P.; Senocrate, A.; Gómez-Camacho, C.E.; Kiefer, F. From CO₂ to Sustainable Aviation Fuel: Navigating the Technology Landscape. *ACS Sustain. Chem. Eng.* **2024**, *12*, 12143–12160. [[CrossRef](#)]
5. Song, C. Global Challenges and Strategies for Control, Conversion and Utilization of CO₂ for Sustainable Development Involving Energy, Catalysis, Adsorption and Chemical Processing. *Catal. Today* **2006**, *115*, 2–32. [[CrossRef](#)]
6. Muradov, N. Low to near-zero CO₂ production of hydrogen from fossil fuels: Status and perspectives. *Int. J. Hydrogen Energy* **2017**, *42*, 14058–14088. [[CrossRef](#)]
7. dos Santos, R.G.; Alencar, A.C. Biomass-derived syngas production via gasification process and its catalytic conversion into fuels by Fischer Tropsch synthesis: A review. *Int. J. Hydrogen Energy* **2020**, *45*, 18114–18132. [[CrossRef](#)]
8. Gutierrez-Martí n, F.; Rodri guez-Anton, L.M. Power-to-SNG technologies by hydrogenation of CO₂ and biomass resources: A comparative chemical engineering process analysis. *Int. J. Hydrogen Energy* **2019**, *44*, 12544–12553. [[CrossRef](#)]
9. Haryanto, A.; Fernando, S.D.; Pordesimo, L.O.; Adhikari, S. Upgrading of syngas derived from biomass gasification: A thermodynamic analysis. *Biomass Bioenergy* **2009**, *33*, 882–889. [[CrossRef](#)]
10. Alauddin, Z.A.B.Z.; Lahijani, P.; Mohammadi, M.; Mohamed, A.R. Gasification of lignocellulosic biomass in fluidized beds for renewable energy development: A review. *Renew. Sustain. Energy Rev.* **2010**, *14*, 2852–2862. [[CrossRef](#)]
11. Dinca, C.; Slavu, N.; Cormos, C.-C.; Badea, A. CO₂ capture from syngas generated by a biomass gasification power plant with chemical absorption process. *Energy* **2018**, *149*, 925–936. [[CrossRef](#)]

12. Zhao, B.; Zhang, X.; Xu, A.; Ding, W.; Sun, L.; Chen, L.; Guan, H.; Yang, S.; Zhou, W. A study of the in-situ CO₂ removal pyrolysis of Chinese herb residue for syngas production. *Sci. Total Environ.* **2018**, *626*, 703–709. [CrossRef] [PubMed]
13. Tijmensen, M.J.A.; Faaij, A.P.C.; Hamelinck, C.N.; Van Hardeveld, M.R.M. Exploration of the possibilities for production of Fischer Tropsch liquids and power via biomass gasification. *Biomass Bioenergy* **2002**, *23*, 129–152. [CrossRef]
14. Ma, J.; Sun, N.; Zhang, X.; Zhao, N.; Xiao, F.; Wei, W.; Sun, Y. A Short Review of Catalysis for CO₂ Conversion. *Catal. Today* **2009**, *148*, 221–231. [CrossRef]
15. Wang, W.; Wang, S.; Ma, X.; Gong, J. Recent Advances in Catalytic Hydrogenation of Carbon Dioxide. *Chem. Soc. Rev.* **2011**, *40*, 3703. [CrossRef]
16. Zhou, Z.; Gao, P. Direct Carbon Dioxide Hydrogenation to Produce Bulk Chemicals and Liquid Fuels via Heterogeneous Catalysis. *Chin. J. Catal.* **2022**, *43*, 2045–2056. [CrossRef]
17. Choi, Y.H.; Jang, Y.J.; Park, H.; Kim, W.Y.; Lee, Y.H.; Choi, S.H.; Lee, J.S. Carbon Dioxide Fischer-Tropsch Synthesis: A New Path to Carbon-Neutral Fuels. *Appl. Catal. B Environ.* **2017**, *202*, 605–610. [CrossRef]
18. Guo, L.; Sun, J.; Ji, X.; Wei, J.; Wen, Z.; Yao, R.; Xu, H.; Ge, Q. Directly converting carbon dioxide to linear α -olefins on bio-promoted catalysts. *Commun. Chem.* **2018**, *1*, 11. [CrossRef]
19. Zhang, K.; Guo, D.; Wang, X.; Qin, Y.; Hu, L.; Zhang, Y.; Zou, R.; Gao, S. Sustainable CO₂ management through integrated CO₂ capture and conversion. *J. CO₂ Util.* **2023**, *72*, 102493. [CrossRef]
20. Zhang, R.; Xie, Z.; Ge, Q.; Zhu, X. Recent advancements in integrating CO₂ capture from flue gas and ambient air with thermal catalytic conversion for efficient CO₂ utilization. *J. CO₂ Util.* **2024**, *89*, 102973. [CrossRef]
21. Latsiou, A.I.; Charisiou, N.D.; Frontistis, Z.; Goula, M.A. From CO₂ to value added chemicals: The promise of single atom catalysts. *Int. J. Hydrogen Energy* **2024**, *92*, 465–481. [CrossRef]
22. Zhang, J.; Ma, L.; Fan, S.; Zhao, T.-S.; Sun, Y. Synthesis of Light Olefins from CO Hydrogenation over Fe–Mn Catalysts: Effect of Carburization Pretreatment. *Fuel* **2013**, *109*, 116–123. [CrossRef]
23. Kuddusi, Y.; Piveteau, L.; Mensi, M.; Cano-Blanco, D.C.; Züttel, A. Selective light olefin synthesis with high ethylene abundance via CO₂ hydrogenation over (Ga-In)2O₃/SSZ-13 catalysts. *J. CO₂ Util.* **2024**, *91*, 103001. [CrossRef]
24. Riedel, T.; Schaub, G.; Jun, K.-W.; Lee, K.-W. Kinetics of CO₂ Hydrogenation on a K-Promoted Fe Catalyst. *Ind. Eng. Chem. Res.* **2001**, *40*, 1355–1363. [CrossRef]
25. Porosoff, M.D.; Yan, B.; Chen, J.G. Catalytic Reduction of CO₂ by H₂ for Synthesis of CO, Methanol and Hydrocarbons: Challenges and Opportunities. *Energy Environ. Sci.* **2016**, *9*, 62–73. [CrossRef]
26. *Green Carbon Dioxide: Advances in CO₂ Utilization*; Centi, G., Perathoner, S., Eds.; Wiley: Hoboken, NJ, USA, 2014. [CrossRef]
27. Dorner, R.W.; Hardy, D.R.; Williams, F.W.; Davis, B.H.; Willauer, H.D. Influence of Gas Feed Composition and Pressure on the Catalytic Conversion of CO₂ to Hydrocarbons Using a Traditional Cobalt-Based Fischer–Tropsch Catalyst. *Energy Fuels* **2009**, *23*, 4190–4195. [CrossRef]
28. Dorner, R.W.; Hardy, D.R.; Williams, F.W.; Willauer, H.D. K and Mn Doped Iron-Based CO₂ Hydrogenation Catalysts: Detection of KAlH₄ as Part of the Catalyst’s Active Phase. *Appl. Catal. A Gen.* **2010**, *373*, 112–121. [CrossRef]
29. Matveyeva, A.N.; Omarov, S.O. Comparison of Perovskite Systems Based on AFeO₃ (A = Ce, La, Y) in CO₂ Hydrogenation to CO. *Trans. Tianjin Univ.* **2024**, *30*, 337–358. [CrossRef]
30. Atta, N.F.; Galal, A.; El-Ads, E.H. Perovskite Nanomaterials—Synthesis, Characterization, and Applications. *Perovskite Mater.–Synth. Characterisation Prop. Appl.* **2016**, 107–151. [CrossRef]
31. Silva, C.L.S.; Marchetti, S.G.; Faro Júnior, A. da C.; de Silva, T.F.; Assaf, J.M.; do Rangel, M.C. Effect of gadolinium on the catalytic properties of iron oxides for WGS. *Catal. Today* **2013**, *213*, 127–134. [CrossRef]
32. Kost, V.V.; Kryuchkova, T.A.; Zimina, V.D.; Sheshko, T.F.; Cherednichenko, A.G.; Kurilkin, V.V.; Safronenko, M.G.; Yafarova, L.V. Catalytic performance of LnFeO₃ complex oxides for dry reforming of methane to synthesis gas. *Bulg. Chem. Commun.* **2019**, *51*, 138–142. Available online: http://bcc.bas.bg/BCC_Content_Volume_51-D_Special.html (accessed on 8 January 2025).
33. Zhang, C.; Jun, K.-W.; Ha, K.-S.; Lee, Y.-J.; Kang, S.C. Efficient Utilization of Greenhouse Gases in a Gas-to-Liquids Process Combined with CO₂ /Steam-Mixed Reforming and Fe-Based Fischer–Tropsch Synthesis. *Environ. Sci. Technol.* **2014**, *48*, 8251–8257. [CrossRef] [PubMed]
34. Rafati, M.; Wang, L.; Shahbazi, A. Effect of Silica and Alumina Promoters on Co-Precipitated Fe–Cu–K Based Catalysts for the Enhancement of CO₂ Utilization during Fischer–Tropsch Synthesis. *J. CO₂ Util.* **2015**, *12*, 34–42. [CrossRef]
35. Sheshko, T.F.; Borodina, E.M.; Yafarova, L.V.; Markova, E.B.; Kryuchkova, T.A.; Cherednichenko, A.G.; Zvereva, I.A.; Terent’ev, A.O. Insights into the Reactivity of Gd_{2–x}Sr_xFe₂O₇ (x = 0 ÷ 0.4) in CO Radical Hydrogenation. *Catalysts* **2023**, *13*, 1256. [CrossRef]
36. Sheshko, T.F.; Markova, E.B.; Sharaeva, A.A.; Kryuchkova, T.A.; Zvereva, I.A.; Chislova, I.V.; Yafarova, L.V. Carbon Monoxide Hydrogenation over Gd(Fe/Mn)O₃ Perovskite-Type Catalysts. *Pet. Chem.* **2019**, *59*, 1307–1313. [CrossRef]

37. Borodina, E.M.; Yafarova, L.V.; Kryuchkova, T.A.; Sheshko, T.F.; Cherednichenko, A.G.; Zvereva, I.A. Influences of Co-Content on the Physico-Chemical and Catalytic Properties of Perovskite $\text{GdCo}_x\text{Fe}_{1-x}\text{O}_3$ in CO Hydrogenation. *Catalysts* **2022**, *13*, 8. [[CrossRef](#)]
38. Marezio, M.; Remeika, J.; Dernier, P. The crystal chemistry of the rare earth orthoferrites. *Acta Crystallogr.* **1970**, *26*, 2008–2022. [[CrossRef](#)]
39. Vasquez, J.A.C.; Téllez, D.A.L.; A Collazos, C.; Rojas, J.R. Structural and magnetic characterization of the new $\text{GdMn}_{1-x}\text{Fe}_x\text{O}_3$ perovskite material. *J. Phys. Conf. Ser.* **2016**, *687*, 012087. [[CrossRef](#)]
40. Khan, H.; Ahmed, J.; Lofland, S.E.; Ramanujachary, K.V.; Ahmad, T. Synergistic Effect of Multiferroicity in GdFeO_3 Nanoparticles for Significant Hydrogen Production through Photo/Electrocatalysis. *Mater. Today Chem.* **2023**, *33*, 101713. [[CrossRef](#)]
41. Graat, P.C.J.; Somers, M.A.J. Simultaneous Determination of Composition and Thickness of Thin Iron-Oxide Films from XPS Fe 2p Spectra. *Appl. Surf. Sci.* **1996**, *100–101*, 36–40. [[CrossRef](#)]
42. Tholkappian, R.; Vishista, K. Tuning the Composition and Magnetostucture of Dysprosium Iron Garnets by Co-Substitution: An XRD, FT-IR, XPS and VSM Study. *Appl. Surf. Sci.* **2015**, *351*, 1016–1024. [[CrossRef](#)]
43. Zhao, K.; Shen, Y.; Huang, Z.; He, F.; Wei, G.; Zheng, A.; Li, H.; Zhao, Z. Different Oxidation Routes for Lattice Oxygen Recovery of Double-Perovskite Type Oxides LaSrFeCoO_6 as Oxygen Carriers for Chemical Looping Steam Methane Reforming. *J. Energy Chem.* **2017**, *26*, 501–509. [[CrossRef](#)]
44. Biesinger, M.C.; Payne, B.P.; Grosvenor, A.P.; Lau, L.W.M.; Gerson, A.R.; Smart, R.S.C. Resolving Surface Chemical States in XPS Analysis of First Row Transition Metals, Oxides and Hydroxides: Cr, Mn, Fe, Co and Ni. *Appl. Surf. Sci.* **2011**, *257*, 2717–2730. [[CrossRef](#)]
45. Uppara, H.P.; Pasupathy, J.S.; Pradhan, S.; Singh, S.K.; Labhsetwar, N.K.; Dasari, H. The Comparative Experimental Investigations of $\text{SrMn}(\text{Co}^{3+}/\text{Co}^{2+})\text{O}_{3\pm\delta}$ and $\text{SrMn}(\text{Cu}^{2+})\text{O}_{3\pm\delta}$ Perovskites towards Soot Oxidation Activity. *Mol. Catal.* **2020**, *482*, 110665. [[CrossRef](#)]
46. Merino, N.A.; Barbero, B.P.; Eloy, P.; Cadús, L.E. $\text{La}_{1-x}\text{Ca}_x\text{CoO}_3$ Perovskite-Type Oxides: Identification of the Surface Oxygen Species by XPS. *Appl. Surf. Sci.* **2006**, *253*, 1489–1493. [[CrossRef](#)]
47. Wang, Y.; Ren, J.; Wang, Y.; Zhang, F.; Liu, X.; Guo, Y.; Lu, G. Nanocasted Synthesis of Mesoporous LaCoO_3 Perovskite with Extremely High Surface Area and Excellent Activity in Methane Combustion. *J. Phys. Chem. C* **2008**, *112*, 15293–15298. [[CrossRef](#)]
48. Sun, J.; Zhao, Z.; Li, Y.; Yu, X.; Zhao, L.; Li, J.; Wei, Y.; Liu, J. Synthesis and Catalytic Performance of Macroporous $\text{La}_{1-x}\text{Ce}_x\text{CoO}_3$ Perovskite Oxide Catalysts with High Oxygen Mobility for Catalytic Combustion of Soot. *J. Rare Earths* **2020**, *38*, 584–593. [[CrossRef](#)]
49. Fuwa, Y.; Wakeshima, M.; Hinatsu, Y. Crystal Structure and Magnetic Properties of a New Layered Cobalt Oxyselenide. *Solid. State Commun.* **2010**, *150*, 1698–1701. [[CrossRef](#)]
50. Yafarova, L.V.; Silyukov, O.I.; Kryuchkova, T.A.; Sheshko, T.F.; Zvereva, I.A. The Influence of Fe Substitution in GdFeO_3 on Redox and Catalytic Properties. *Russ. J. Phys. Chem.* **2020**, *94*, 2679–2684. [[CrossRef](#)]
51. Kang, S.C.; Jun, K.-W.; Lee, Y.-J. Effects of the CO/CO₂ Ratio in Synthesis Gas on the Catalytic Behavior in Fischer–Tropsch Synthesis Using K/Fe–Cu–Al Catalysts. *Energy Fuels* **2013**, *27*, 6377–6387. [[CrossRef](#)]
52. Sonal Ahmad, E.; Upadhyayula, S.; Pant, K.K. Biomass-Derived CO₂ Rich Syngas Conversion to Higher Hydrocarbon via Fischer-Tropsch Process over Fe–Co Bimetallic Catalyst. *Int. J. Hydrogen Energy* **2019**, *44*, 27741–27748. [[CrossRef](#)]
53. Wang, Z.X.; Dong, T.; Yuan, L.X.; Kan, T.; Zhu, X.F.; Torimoto, Y.; Sadakata, M.; Li, Q.X. Characteristics of Bio-Oil-Syngas and Its Utilization in Fischer–Tropsch Synthesis. *Energy Fuels* **2007**, *21*, 2421–2432. [[CrossRef](#)]
54. Yao, Y.; Liu, X.; Hildebrandt, D.; Glasser, D. The Effect of CO₂ on a Cobalt-Based Catalyst for Low Temperature Fischer–Tropsch Synthesis. *Chem. Eng. J.* **2012**, *193–194*, 318–327. [[CrossRef](#)]
55. Daza, Y.A.; Kuhn, J.N. CO₂ Conversion by Reverse Water Gas Shift Catalysis: Comparison of Catalysts, Mechanisms and Their Consequences for CO₂ Conversion to Liquid Fuels. *RSC Adv.* **2016**, *6*, 49675–49691. [[CrossRef](#)]
56. Álvarez, A.; Bansode, A.; Urakawa, A.; Bavykina, A.V.; Wezendonk, T.A.; Makkee, M.; Gascon, J.; Kapteijn, F. Challenges in the Greener Production of Formates/Formic Acid, Methanol, and DME by Heterogeneously Catalyzed CO₂ Hydrogenation Processes. *Chem. Rev.* **2017**, *117*, 9804–9838. [[CrossRef](#)] [[PubMed](#)]
57. Ma, Z.; Porosoff, M.D. Development of Tandem Catalysts for CO₂ Hydrogenation to Olefins. *ACS Catal.* **2019**, *9*, 2639–2656. [[CrossRef](#)]
58. Ronda-Lloret, M.; Rothenberg, G.; Shiju, N.R. A Critical Look at Direct Catalytic Hydrogenation of Carbon Dioxide to Olefins. *ChemSusChem* **2019**, *12*, 3896–3914. [[CrossRef](#)]
59. Visconti, C.G.; Lietti, L.; Tronconi, E.; Forzatti, P.; Zennaro, R.; Finocchio, E. Fischer–Tropsch Synthesis on a Co/Al₂O₃ Catalyst with CO₂ Containing Syngas. *Appl. Catal. A Gen.* **2009**, *355*, 61–68. [[CrossRef](#)]
60. Liang, B.; Sun, T.; Ma, J.; Duan, H.; Li, L.; Yang, X.; Zhang, Y.; Su, X.; Huang, Y.; Zhang, T. Mn Decorated Na/Fe Catalysts for CO₂ Hydrogenation to Light Olefins. *Catal. Sci. Technol.* **2019**, *9*, 456–464. [[CrossRef](#)]

61. Kulikova, M.V.; Chudakova, M.V.; Ivantsov, M.I.; Dementyva, O.S.; Maksimov, A.L. Hydrocarbon Synthesis from CO₂ and H₂ Using the Ultrafine Iron-Containing Catalytic Systems Based on Carbonized Cellulose. *Eurasian Chem. Tech. J.* **2022**, *24*, 149. [[CrossRef](#)]
62. Al-Dossary, M.; Ismail, A.A.; Fierro, J.L.G.; Bouzid, H.; Al-Sayari, S.A. Effect of Mn Loading onto MnFeO Nanocomposites for the CO₂ Hydrogenation Reaction. *Appl. Catal. B Environ.* **2015**, *165*, 651–660. [[CrossRef](#)]
63. Bligaard, T.; Honkala, K.; Logadottir, A.; Nørskov, J.K.; Dahl, S.; Jacobsen, C.J.H. On the Compensation Effect in Heterogeneous Catalysis. *J. Phys. Chem. B* **2003**, *107*, 9325–9331. [[CrossRef](#)]
64. Mota, N.; Millán Ordoñez, E.; Pawelec, B.; Fierro, J.L.G.; Navarro, R.M. Direct Synthesis of Dimethyl Ether from CO₂: Recent Advances in Bifunctional/Hybrid Catalytic Systems. *Catalysts* **2021**, *11*, 411. [[CrossRef](#)]
65. Kryuchkova, T.A.; Kost', V.V.; Sheshko, T.F.; Chislova, I.V.; Yafarova, L.V.; Zvereva, I.A. Effect of Cobalt in GdFeO₃ Catalyst Systems on Their Activity in the Dry Reforming of Methane to Synthesis Gas. *Pet. Chem.* **2020**, *60*, 609–615. [[CrossRef](#)]
66. Malhi, H.S.; Sun, C.; Zhang, Z.; Liu, Y.; Liu, W.; Ren, P.; Tu, W.; Han, Y.-F. Catalytic Consequences of the Decoration of Sodium and Zinc Atoms during CO₂ Hydrogenation to Olefins over Iron-Based Catalyst. *Catal. Today* **2022**, *387*, 28–37. [[CrossRef](#)]
67. Tu, W.; Ghossoub, M.; Singh, C.V.; Chin, Y.-H.C. Consequences of Surface Oxophilicity of Ni, Ni-Co, and Co Clusters on Methane Activation. *J. Am. Chem. Soc.* **2017**, *139*, 6928–6945. [[CrossRef](#)] [[PubMed](#)]
68. Sadykov, V.A.; Bulgakov, N.N.; Muzykantov, V.S.; Kuznetsova, T.G.; Alikina, G.M.; Lukashevich, A.I.; Neophytides, S. Mobility and reactivity of the surface and lattice oxygen of some complex oxides with perovskite structure. In *Mixed Ionic Electronic Conducting Perovskites for Advanced Energy Systems*; Springer: Dordrecht, The Netherlands, 2004; Volume 183, pp. 53–74. [[CrossRef](#)]
69. Goguet, A.; Meunier, F.C.; Tibiletti, D.; Breen, J.P.; Burch, R. Spectrokinetic Investigation of Reverse Water-Gas-Shift Reaction Intermediates over a Pt/CeO₂ Catalyst. *J. Phys. Chem. B* **2004**, *108*, 20240–20246. [[CrossRef](#)]
70. Mebel, A.M.; Hwang, D.-Y. Theoretical Study on the Reaction Mechanism of Nickel Atoms with Carbon Dioxide. *J. Phys. Chem. A* **2000**, *104*, 11622–11627. [[CrossRef](#)]
71. Popova, N.M.; Babenkova, L.V.; Savel'eva, G.A. *Adsorption and Interaction of the Simplest Gases with VIII Group Metals*; Nauka: Alma-Ata, Kazakhstan, 1979; pp. 83–97. (In Russian)
72. Weber, D.; He, T.; Wong, M.; Moon, C.; Zhang, A.; Foley, N.; Ramer, N.J.; Zhang, C. Recent Advances in the Mitigation of the Catalyst Deactivation of CO₂ Hydrogenation to Light Olefins. *Catalysts* **2021**, *11*, 1447. [[CrossRef](#)]
73. Li, W.H.; Wang, H.Z.; Jiang, X.; Zhu, J.; Liu, Z.M.; Guo, X.W.; Song, C.S. A short review of recent advances in CO₂ hydrogenation to hydrocarbons over heterogeneous catalysts. *RCS Adv.* **2018**, *8*, 7651–7669. [[CrossRef](#)]
74. Chislova, I.V.; Matveeva, A.A.; Volkova, A.V.; Zvereva, I.A. Sol-Gel Synthesis of Nanostructured Perovskite-like Gadolinium Ferrites. *Glass Phys. Chem.* **2011**, *37*, 653–660. [[CrossRef](#)]
75. Yafarova, L.V.; Chislova, I.V.; Zvereva, I.A.; Kryuchkova, T.A.; Kost, V.V.; Sheshko, T.F. Sol-gel synthesis and investigation of catalysts on the basis of perovskite-type oxides GdMO₃ (M = Fe, Co). *J. Sol-Gel Sci. Technol.* **2019**, *92*, 264–272. [[CrossRef](#)]

Disclaimer/Publisher's Note: The statements, opinions and data contained in all publications are solely those of the individual author(s) and contributor(s) and not of MDPI and/or the editor(s). MDPI and/or the editor(s) disclaim responsibility for any injury to people or property resulting from any ideas, methods, instructions or products referred to in the content.